Bio-inspired overlapping curl structures for toughening bio-based epoxy
A study on the fracture phenomena

Xu, Zhiyuan; Tao, Ran; Masania, Kunal; Teixeira de Freitas, Sofia

DOI
10.1016/j.compscitech.2025.111374

Publication date
2025

Document Version
Final published version

Published in
Composites Science and Technology

Composites Science and Technology 272 (2025) 111374

Contents lists available at ScienceDirect

Composites Science and Technology

journal homepage: www.elsevier.com/locate/compscitech

Bio-inspired overlapping curl structures for toughening bio-based epoxy: A study on the fracture phenomena

Zhiyuan Xu [a], Ran Tao [a], Kunal Masania [b,*], Sofia Teixeira de Freitas [a,c,**]

[a] Faculty of Aerospace Engineering, Delft University of Technology, Delft 2629 HS, Netherlands
[b] Shaping Matter Lab, Faculty of Aerospace Engineering, Delft University of Technology, Delft 2629 HS, Netherlands
[c] IDMEC, Instituto Superior Técnico, Universidade de Lisboa, Lisboa, Portugal

ARTICLE INFO

Dataset link: https://doi.org/10.4121/ff4882ad-4cd6-49d3-8878-623c6b712759

Keywords:
Bio-inspired
Bio-based epoxy
Toughening mechanisms
Fracture

ABSTRACT

In this study, a 3D-printed biomimetic overlapping curl structure inspired by spider silk molecular structure, containing sacrificial bonds and hidden lengths, is studied as a toughening mechanism for a bio-based epoxy. Experimental results of the fracture phenomena of the overlapping curl-reinforced bio-based epoxy identify three toughening mechanisms triggered by the overlapping curl: (1) crack re-initiation, (2) overlapping curl bridging, and (3) epoxy ligament. First, the integrated overlapping curl creates a void within the epoxy matrix. As the crack tip reaches the end of this void, the crack re-initiates. Then, as the hidden length of overlapping curl unfolds, it leads to a bridging effect in resisting crack growth. In addition, for the smallest hidden length, an epoxy ligament is formed due to crack branching, significantly improving the energy release rate. The epoxy fracture energy release rate increased by 13 %. The overall modest improvement is attributed to the large plastic dissipation energy of the epoxy and the relatively low overlapping curl load-capacity. However, when expanding the design space numerically, it was shown that as the failure load of the overlapping curl increases, the bridging effect increases progressively. The introduction of the bio-inspired overlapping curl structure into bio-based epoxy proves the concept of a toughening strategy for developing high-performance sustainable composite materials.

1. Introduction

Thanks to its high stiffness, good corrosion resistance, and high strength, thermoset epoxy has been widely used in engineering materials, such as composites [1,2], adhesives [3,4], coatings [5], etc. Currently, the majority of the commercially available epoxy resins are derived from petroleum resources [6,7]. The environmental impact and dependency on non-renewable resources require more sustainable alternatives. Attention has been paid to the green and environmental-friendly epoxy. The bio-based epoxy resins, synthesized from renewable resources such as lignin, soybean oil, or cashew phenol, offer sustainability advantages, reduced carbon emissions, and biodegradability [3,7]. However, their mechanical properties and thermal stability often underperform compared to petroleum-based counterparts [8–10], posing challenges for high-performance application.

Reported works indicated that structural hierarchies in materials can contribute to the toughness, which can be classified as intrinsic (from atomic to nanoscale) and extrinsic (from micro to macroscale) toughening mechanisms [11,12]. During crack propagation, the intrinsic toughening operates ahead of the crack tip, relying more on the plasticity and enlarging the fracture process zone of the materials. Introducing micro-rubber particles or silica nano-particles to increase plasticity and enlarge the plastic zone has shown a significant increase in the epoxy toughness and effective against crack initiation and propagation [13].

Compared with intrinsic toughening, extrinsic toughening mechanisms act mostly behind the crack tip to inhibit crack propagation, mainly including bridging, fiber pull-out, and crack path deflection [14–16], which is efficient in resisting crack growth. Researchers have endorsed a lot of efforts to explore this area in pursuit of achieving greater toughness. For example, van Innis et al. [14] inserted polyethylene filaments acting as bridging ligaments into co-cured composite joints to improve the toughness by 3 times. Similarly, Tao et al. [17] applied laser-based surface treatment to secondary bonded composite joints, triggering adhesive ligament bridging and achieving toughness improvement. Besides, the integrated fiber or carbon nanotube pullout mechanisms can also dissipate much fracture energy in composites, delaying crack propagation [15,18,19]. Also, architecture design in the

* Corresponding author.
** Corresponding author at: Faculty of Aerospace Engineering, Delft University of Technology, Delft 2629 HS, Netherlands.
E-mail addresses: k.masania@tudelft.nl (K. Masania), s.teixeiradefreitas@tudelft.nl (S. Teixeira de Freitas).

https://doi.org/10.1016/j.compscitech.2025.111374
Received 16 July 2025; Received in revised form 31 August 2025; Accepted 6 September 2025
Available online 16 September 2025

topology geometries of bulk material, e.g., sacrificial cuts, are able to deflect the crack path to increase the toughness [16,20,21].

Natural materials have spontaneously evolved into lightweight materials with high strength and toughness, containing a mutual of intrinsic and extrinsic toughening mechanisms. For example, in nacre, the fracture toughness is several orders higher than the mineral constituents through a "brick-and-mortar" structure where brittle mineral platelets are separated by organic proteins that allow limited sliding to relieve stress. This sliding enables the tortuous crack deflection along rough platelet surfaces and platelet pull-out, which further enhances toughness [11,22]. Another prime natural material is spider silk, its exceptional strength and toughness come from its unique sacrificial bonds and hidden lengths toughening mechanism within its protein microstructure [23,24]. By breaking the sacrificial bonds, such as hydrogen bonds, energy is dissipated under stress. Moreover, the uncoiling and stretching of hidden lengths enhances its toughness further, making it both strong and highly extensible.

Many scientists are working to decipher and mimic these biological structures to develop fracture-resistant and high-performance materials, such as synthesized fibers [23,24], adhesives [25], 3D-printed junctions [26], glass [27], and composites [28,29]. Mazzota et al. [25] incorporated organic functional additives into adhesive to create interpolymeric networks containing weak sacrificial hydrogen bonds. These sacrificial bonds can easily break under stress, allowing effective dissipation of mechanical energy while maintaining the integrity of the matrix, significantly improving the toughness of the adhesive. Similarly, Zou et al. [30,31] utilized 3D printing technology to replicate the structure of the sacrificial bonds and hidden lengths on the macroscale using a molten polymer filament. By integrating these physical structures into elastomers, they demonstrated the toughening mechanisms where the sacrificial bonds break and the hidden lengths subsequently unfold [32]. This approach led to remarkable improvements, including a ~17-fold increase in stiffness and a ~7-fold increase in total energy to failure compared to the neat elastomer. Despite these achievements, the application of the macroscale sacrificial bonds and hidden lengths structure in epoxy material remains unexplored. The primary challenge lies in engineering these structures to function effectively under low strain values, typical of structural epoxies, and simultaneously ensure that the sacrificial bonds break and the hidden lengths unfold to produce meaningful bridging effects.

In this work, inspired by the microstructure of spider silk, 3D-printed overlapping curl fibers consisting of sacrificial bonds and hidden lengths, are impregnated within the bio-based epoxy matrix. The effects of the overlapping curl geometry on the fracture process and its toughening mechanisms are studied. In addition, the bridging effects of the overlapping curl on the epoxy are simulated by the finite element method to better understand the key toughening mechanisms. This work is a proof of concept of the promising bio-inspired overlapping curl structure to toughen bio-based epoxy, enabling to achieve a strong, tough, and sustainable composite material.

2. Materials and experimental methodology

2.1. 3D-printed overlapping curls

The overlapping curl (OC) structures containing sacrificial bonds and hidden lengths were additively manufactured using commercial polylactic acid filament (PLA, ReForm™ - rPLA, Formfutura BV, Nijmegen, Netherlands). A 3D printer Prusa i3 MK3S+ with a nozzle size $0.8\,\mathrm{mm}$ was used for fused filament fabrication to obtain coiling fibers with sacrificial bonds and hidden lengths via the coiling rope effect [33], as shown in Fig. 1(a). The $0.8\,\mathrm{mm}$ nozzle was specifically selected because it enables the fabrication of OCs with superior mechanical properties based on our previous work [31], making them more effective as reinforcements for the epoxy matrix. By adjusting the custom-written g code containing the moving speed of the nozzle F, the extrusion value of the filament E and the height of the nozzle Z, different overlapping curl patterns were fabricated. Two different nozzle heights, $Z = 10\,\mathrm{mm}$ and $Z = 5\,\mathrm{mm}$, were used to print overlapping curls showing distinct hidden lengths and mechanical properties, with the aim of assessing their comparative toughening effects on the epoxy matrix. The overlapping curl structures were named by the nozzle height: OC_Z10 and OC_Z5. OC_Z10 has a larger curl size than OC_Z5 and the diameter d of the overlapping curl fiber is approximately $0.98\,\mathrm{mm}$ for both geometries. As a benchmark, a straight fiber with a similar diameter was also printed to be used as a reference. Fig. 1(b) and Table 1 show the overlapping curl structure and the corresponding 3D-printing parameters and geometry.

2.2. Bio-based epoxy resin

For the matrix, a two-component bio-based epoxy (SR GreenCast 160 for matrix/SD 7160 for hardener) was used and mixed in a mixing ratio of 1:0.42 [34]. The mixture was placed into a vacuum chamber for degassing around 1 h and, subsequently, poured into the designed silicon mold to manufacture tensile and compact tension (CT) specimens with a consistent geometry, as shown in Fig. 2(a) and (b). The epoxy resin was cured for 7 days at room temperature before testing as recommended by the technical datasheet [34]. Note worth it that the epoxy resin was purposefully chosen as transparent to allow a visual observation of the fracture phenomena when the OC structures are impregnated in the resin.

2.3. Experimental methods

2.3.1. Single overlapping curl tensile test

A universal Zwick loading frame with $100\,\mathrm{N}$ loadcell was used to characterize the mechanical properties of the 3D-printed PLA straight fiber and overlapping curl. It is worth noting that only one curl was tested, as only one sacrificial bond tended to break in the CT specimens. For details in specimen preparation and testing procedures, please refer to [31]. The testing speed was set to $2\,\mathrm{mm/min}$ and at least five specimens were tested for each configuration.

2.3.2. Tensile test of the epoxy resin

Tensile dog-bone specimens of the pure epoxy (without OC) were tested following the standard ISO-527 [35] to characterize the epoxy mechanical properties. The average ± standard deviation thickness of specimens was $4.46 \pm 0.18\,\mathrm{mm}$ (the nominal thickness was $4\,\mathrm{mm}$). A universal Zwick loading frame with $10\,\mathrm{kN}$ loadcell was used for the tensile test of epoxy resin and 3D Digital Image Correlation (DIC) was used to record the deformation. To enable the DIC evaluation, a thin layer of white paint was applied to the front of the specimens with the black speckles painted on top. The 3D image acquisition system was placed facing the specimen (VIC-3D system by Correlated Solutions, Inc.) with pictures taken every two seconds after the load application. The testing speed was $2\,\mathrm{mm/min}$ and four specimens were tested.

2.3.3. Compact tension test

Compact tension tests were performed to characterize and evaluate the fracture phenomena triggered by the OC when impregnated into the biobased epoxy resin. Four types of CT specimens were tested: CT-Pure, with only the epoxy resin without any reinforcement, CT-Straight, with one straight fiber impregnated within the epoxy resin, CT-OC_Z10, with one OC_Z10 impregnated within the epoxy resin and CT-OC_Z5, with one OC_Z5 impregnated within the epoxy resin. Owing to current 3D-printing constraints, millimeter-scale OCs were used, with a single OC incorporated per specimen to demonstrate the OC-toughening mechanism in structural epoxy. Staples were inserted into the mold to serve as anchoring points, fixing the two ends of these reinforcements and maintaining their position at the mid-thickness of the specimen. In CT-OC_Z10 and CT-OC_Z5, the OC was oriented perpendicular to

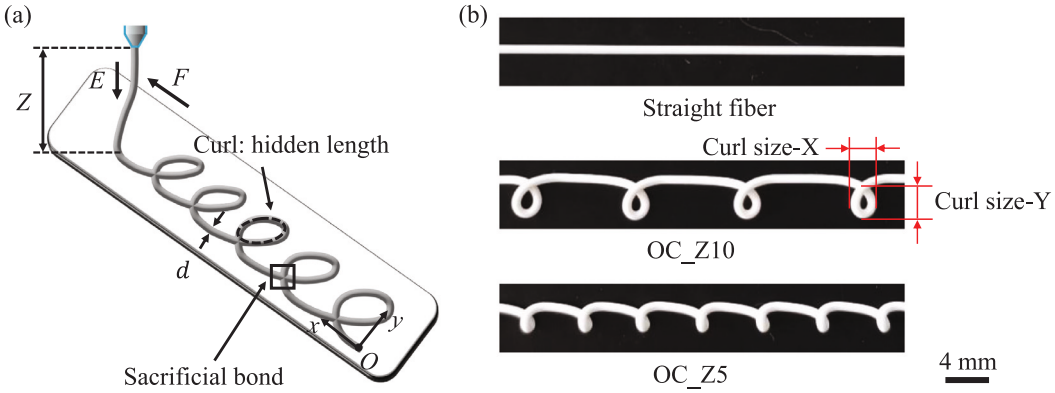

Fig. 1. (a) The 3D-printing process schematic of overlapping curl fabrication. (b) The geometry of printed PLA straight fiber and overlapping curl structures.

Table 1
3D-printing parameters and geometry of the straight fiber and overlapping curls. Z: nozzle height, F: nozzle moving speed, and E: filament extrusion value (average ± std).

Nomenclature	Z (mm)	F (mm/min)	E (mm/min)	Curl size-X (mm)	Curl size-Y (mm)
Straight	10	1000	60	–	–
OC_Z10	10	610	130	3.55 ± 0.08	4.08 ± 0.09
OC_Z5	5	610	130	1.93 ± 0.03	2.30 ± 0.08

the crack path with one curl aligned with the centerline of the crack path. To ensure that the overlapping curl fully unfolds and breaks within the crack propagation region of the CT, standard CT geometry specified in [36] and ASTM D5045 [37] was modified by using a larger CT specimen, as shown in Fig. 2(b). In this modified geometry, the dimension $W - a_0$ is 48 mm, compared to 15 mm in the standard CT geometry, where W is the specimen width and a_0 is the initial crack length. This modification has implications in terms of output, since the results will no longer represent a material property, guaranteed by the standard CT, but a modified-geometric property. Nevertheless, this modified geometry ensures that the fracture phenomena triggered by the OC are fully developed, and fully analyzes its implication on the crack propagation region. The nominal thickness of the CT specimens was 8 mm. After 7 days of curing, the average ± standard deviation thicknesses of the CT specimens were: CT-Pure: 7.83 ± 0.16 mm, CT-Straight: 7.70 ± 0.36 mm, CT-OC_Z10: 7.93 ± 0.24 mm, and CT-OC_Z5: 8.14 ± 0.23 mm. A universal Zwick loading frame with 10 kN loadcell and DIC cameras were used for the compact tension test. Besides, on the opposite side surface of the CT specimen, a traveling microscope was used to observe the crack propagation in-situ. The mechanical test set-up for compact tension test is shown in Fig. 2(c). The testing speed was 2 mm/min. Five CT specimens of each configuration were tested.

The energy release rate (ERR) of the CT specimens was calculated based on the following compliance method [38],

$$\mathrm{ERR} = \frac{P^2}{2t}\frac{\mathrm{d}C}{\mathrm{d}a} \tag{1}$$

where P is the load, t is the specimen thickness, C is the compliance as a polynomial function of crack length a, that is $C = (\alpha a + \beta)^n$. α, β, and n are calculated to best fit the experimental data.

3. Experimental results

3.1. Single overlapping curl tensile test results

Fig. 3 shows the representative load versus displacement curves of the 3D-printed structures: straight, OC_Z10 and OC_Z5. Under tension, the sacrificial bond of the overlapping curl first breaks (point **i**), followed by a load drop ending at F_h. As the hidden length unfolds, the load raises again (e.g., points **ii** and **iii**) until it reaches the ultimate failure load F_u (point **iv**) where the fiber breaks. The straight fiber only shows a constant increase in the load until a sudden break, represented by the peak load. While comparing these load versus displacement curves, one can clearly observe the advantage of OC compared to the straight fiber, as more energy is absorbed as a consequence of the hidden length unfolding. Table 2 lists the holding force F_h, the ultimate load F_u, and the hidden length l for the three configurations. The average holding load F_h of OC_Z5 (10.47 N) is higher than that of OC_Z10 (3.06 N). This is mainly due to the fact that the smaller curl size OC_Z5 shows more structure rigidity when compared to OC_Z10 [31]. However, due to a longer hidden length, OC_Z10 exhibits a higher F_u compared to OC_Z5. Moreover, a higher stiffness is observed in OC_Z5 than in OC_Z10 within the displacement range of 0.85 to 5.65 mm. Beyond this displacement, OC_Z10 becomes stiffer. For further understanding of the effect of the geometry of the OC on its mechanical properties, please refer to [31].

Table 2
PLA straight fiber and overlapping curl mechanical parameters. F_h: holding load; F_u: ultimate failure load; l: hidden length (average ± std).

Nomenclature	F_h (N)	F_u (N)	l (mm)
Straight	–	35.25 ± 0.76	–
OC_Z10	3.06 ± 0.31	35.14 ± 1.60	12.73 ± 0.70
OC_Z5	10.47 ± 0.45	22.18 ± 0.92	4.81 ± 0.13

3.2. Tensile properties of the bio-based epoxy resin

Fig. 4 shows the representative stress–strain curve of the bio-based epoxy under the uniaxial tensile test and the corresponding mechanical properties are summarized in Table 3.

3.3. Compact tension test

3.3.1. Integration of PLA straight fiber

Fig. 5 compares the representative results of the compact tension tests of the specimens containing a straight fiber (CT-Straight) and with no reinforcement, i.e., pure (CT-Pure). Fig. 5(a) compares the representative normalized load versus displacement curves of the CT-Pure and CT-Straight. The load was normalized to the thickness of each

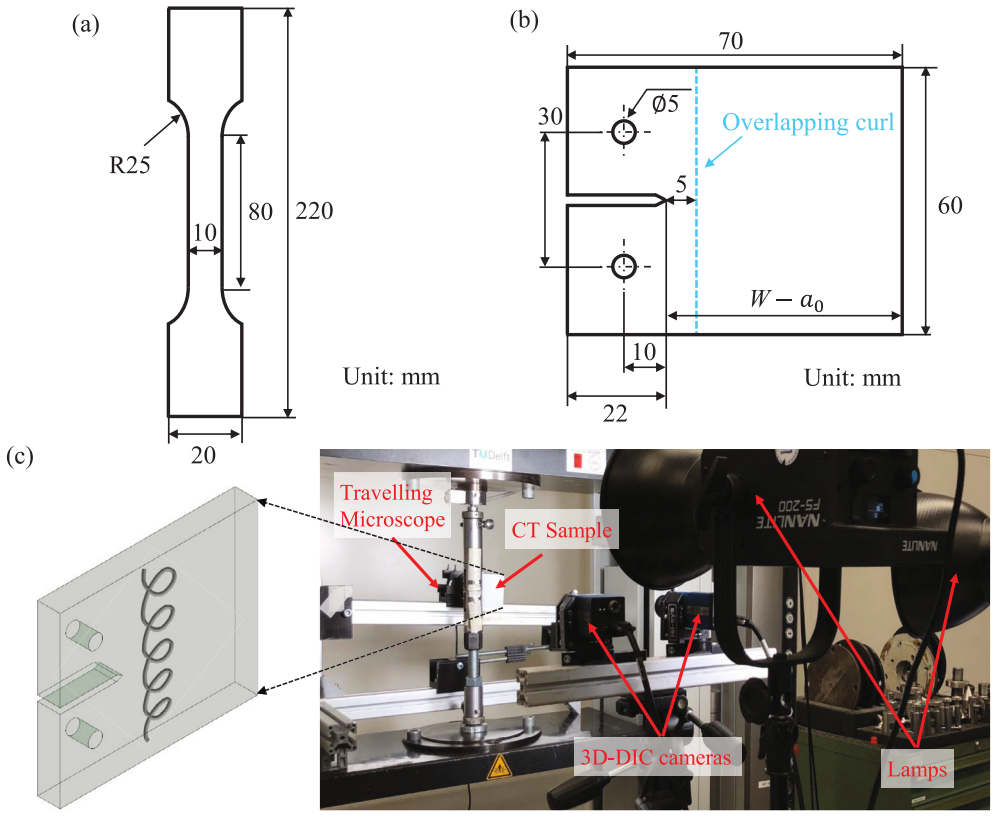

Fig. 2. The geometry and dimensions of (a) the tensile dog-bone specimen (nominal thickness of 4 mm) and (b) the CT specimen (nominal thickness of 8 mm). The blue dashed line represents the position of the embedded straight fiber or overlapping curl structure. (c) The mechanical test setup for the compact tension test.

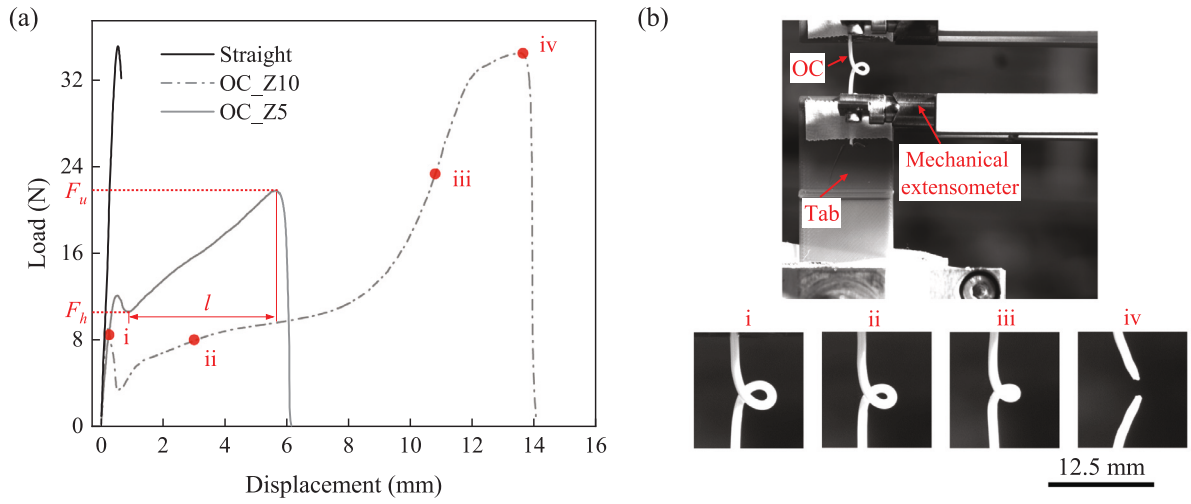

Fig. 3. (a) The load versus displacement curves of PLA straight fiber and overlapping curls with only one curl. F_h: the holding load after the sacrificial bond break; F_u: ultimate failure load. l: the hidden length due to the curl unfolding, defined as the distance between F_h and F_u. (b) The corresponding deformation process of OC_Z10. Point **i** is the break of the sacrificial bond, points **ii** and **iii** are the hidden length unfolding process, and point **iv** is the final failure of the overlapping curl structure.

specimen to eliminate the small differences between the specimens: $\overline{P} = P/t$. The two curves show very similar behavior. However, with the integrated straight fiber, the normalized load has a slight increase from point 1 to point 6, showing that there is an effect of straight fiber, possibly withstanding part of the load. This is confirmed by a sudden load drop at point 6 when the straight fiber breaks, as indicated by the red circle and confirmed by picture 6-Fig. 5(d). Fig. 5(d) shows the fracture process of the CT-Straight. After the crack passes the straight fiber (point 2), the straight fiber starts to neck until the final break at point 6. The crack length and energy release rate results are also shown in Fig. 5(b) and (c). Both the crack propagation rate and the ERR of the CT-Straight show similar values to those of CT-Pure. Even with the breaking of the straight fiber at point 6, the ERR remains the same as the CT-Pure. The average ERR values were taken from the crack length of 15.5 mm to 25.2 mm (the range of reinforcement influence until the ERR starts to decline). The average energy release rate values are

Table 3
Mechanical properties of Greencast epoxy resin (average ± std).

Young's modulus (MPa)	σ_{yield} (MPa)[a]	$\sigma_{strength}$ (MPa)[b]	$\sigma_{fracture}$ (MPa)[c]	$\epsilon_{fracture}$ (mm/mm)[d]
666.87 ± 80.36	5.07 ± 0.09	12.44 ± 0.53	11.63 ± 0.22	0.44 ± 0.08

[a] The yield stress is defined as the elastic limit in the stress–strain curve.
[b] The maximum stress in the stress–strain curve.
[c] The stress at which the specimen fractures.
[d] The strain at which the specimen fractures.

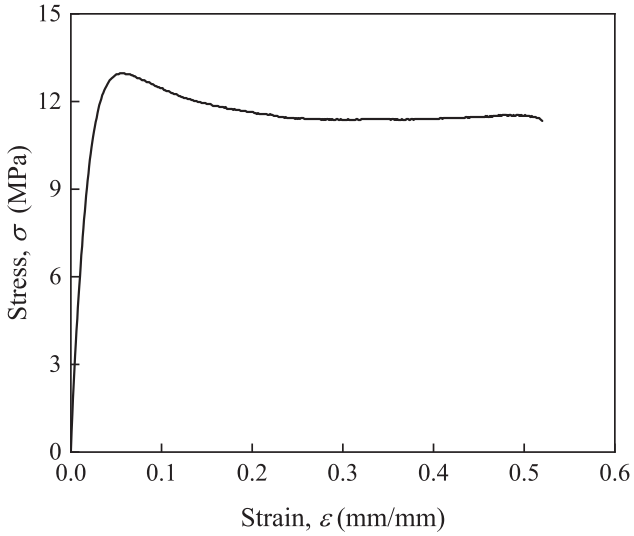

Fig. 4. The representative engineering stress–strain curve of the epoxy resin.

80.79 ± 4.67 kJ/mm^2 and 80.79 ± 2.16 kJ/mm^2 for CT-Pure and CT-Straight, respectively. These results show that the integrated straight fiber has limited effects on delaying crack propagation and improving the ERR of the epoxy.

3.3.2. Integration of PLA overlapping curl

Fig. 6 shows the representative overall results of the series CT-OC_Z10. The CT-Pure results are also plotted as a reference. From Fig. 6(a), one can observe that, when compared to the CT-Pure, in the CT-OC_Z10, there is an abrupt load drop after the peak load (marked by a triangle in the load–displacement curve). The inserted figure in the plot marked with a triangle shows a close up of the region of the crack tip at this load drop. As the crack starts to propagate, one can observe an opening gap between the epoxy and OC before the crack tip reaches the OC. This void affects the integrity of the surrounding epoxy matrix and leads to a load drop marked by the triangle in the load–displacement curve up to point 1 when the crack reaches the OC. With the crack propagating further, the OC starts to unfolds and withstands a residual load behind the crack tip (from Fig. 6(d)-point 2 to point 6). As a result of this OC-effect, the CT-OC_Z10 shows a higher load than CT-Pure at the same displacement. In Fig. 6(b), it is shown that from crack length $a > 18$ mm, there is a 8% decrease in crack propagation due to this overlapping curl effect compared to the CT-Pure - highlighted in the gray. As a result, the energy release rate values for CT-OC_Z10 increase to 88.65 ± 5.05 kJ/m^2 between $a = 15.5$ mm to $a = 25$ mm in comparison with 80.79 ± 4.67 kJ/m^2 in the pure specimen. At points 5 and 6, however, the toughening effect is no longer significant.

Fig. 7 shows the representative overall results of CT-OC_Z5. The CT-Pure results are also plotted as a reference. In Fig. 7(a), a similar load drop also occurs after the peak load as in CT-OC_Z10, but is less pronounced. As the crack tip reaches the OC (point 1), the slope decreases significantly as the OC starts to share part of the carrying load. This is again shown by a higher load than CT-Pure at the same displacement. Due to the smaller curl size of OC_Z5, the hidden length is shorter and the OC breaks at lower crack length 23.5 mm when compared to OC_Z10 (Fig. 7(d)-point 4). The OC_Z5 also demonstrates crack delaying ability in epoxy with a decrease of 11% on the crack propagation, as shown in Fig. 7(b). This also has a significant effect on the average ERR values of CT-OC_Z5 91.03 ± 5.45 kJ/m^2 - see Fig. 7(c). From Fig. 7(d)-point 3, we observe an epoxy ligament to form and develop. The ERR remains higher than the CT-Pure through the whole crack propagation. Contrary to CT-OC_Z10, even after the ERR values start to decline ($a > 27.5$ mm), the values of the CT-OC_Z5 do not collapse with the values of CT-Pure. The obtained ERR values for all CT configurations are summarized in Table 4. Among the integrated PLA structure reinforcements, the OC_Z5 results in the largest improvement of the energy release rate of the epoxy by 13%. It is important to note that, after testing, a significant plastic deformation was present in the CT-specimens; therefore, the energy release rate, which includes both elastic and plastic contributions, should only be used as a comparative indicator across different specimens and not as an absolute value of fracture toughness. The calculated ERR values reflect the combined effects of elastic and plastic energy dissipation and are suitable for assessing the relative improvements between different designs.

Table 4
Summary of energy release rate of the compact tension specimens (average ± std).

Nomenclature	CT-Pure	CT-Straight	CT-OC_Z10	CT-OC_Z5
Energy release rate, ERR (kJ/m^2)	80.79 ± 4.67	80.79 ± 2.16	88.65 ± 5.05	91.03 ± 5.45

Table 5
The roughness of the CT fracture surface along representative lines as listed in Fig. 8. R_a: Arithmetic average of profile height along selected lines.

Ra (μm)	Line i	Line ii	Line iii	Average ± std
CT-Pure	39.0 ± 0.2	40.2 ± 0.1	36.6 ± 0.2	38.6 ± 0.1
CT-Straight	100.1 ± 0.3	80.8 ± 1.9	56.6 ± 0.1	79.2 ± 0.6
CT-OC_Z10	107.9 ± 6.9	66.8 ± 0.3	79.3 ± 0.4	84.7 ± 2.3
CT-OC_Z5	313.1 ± 1.4	398.9 ± 9.6	437.2 ± 1.4	383.1 ± 3.3

3.3.3. Toughening mechanisms by in-situ observations

To better understand and analyze the CT fracture process and toughening mechanisms triggered by the embedded OC that affect the ERR, Fig. 8 shows for each CT-series, in-situ photos of the crack tip, the corresponding energy release rate data points, and the fracture surface topography taken after testing. The CT-Pure result is shown as a reference.

In the CT specimens with impregnated OC, CT-OC_Z10 and CT-OC_Z5, as the crack tip starts to propagate, the first disturbance that encounters is a void created by the curl of OC. With the integration of a reinforcement structure like OCs, a void is created in the epoxy matrix along the boundaries of the curl. The voids created by the OCs are clearly visible before the crack passes by the OC (point 1 of Fig. 8(c) and (d)), and post mortem on the fracture surfaces, as outlined by the white dashed ellipses in Fig. 8(c) and (d). As the crack reaches the void, there is a load drop identified both in CT-OC_Z10 and CT-OC_Z5 — see Figs. 6(a) and 7(a). After passing the void, the crack re-initiates, leading to the redevelopment of the fracture process zone.

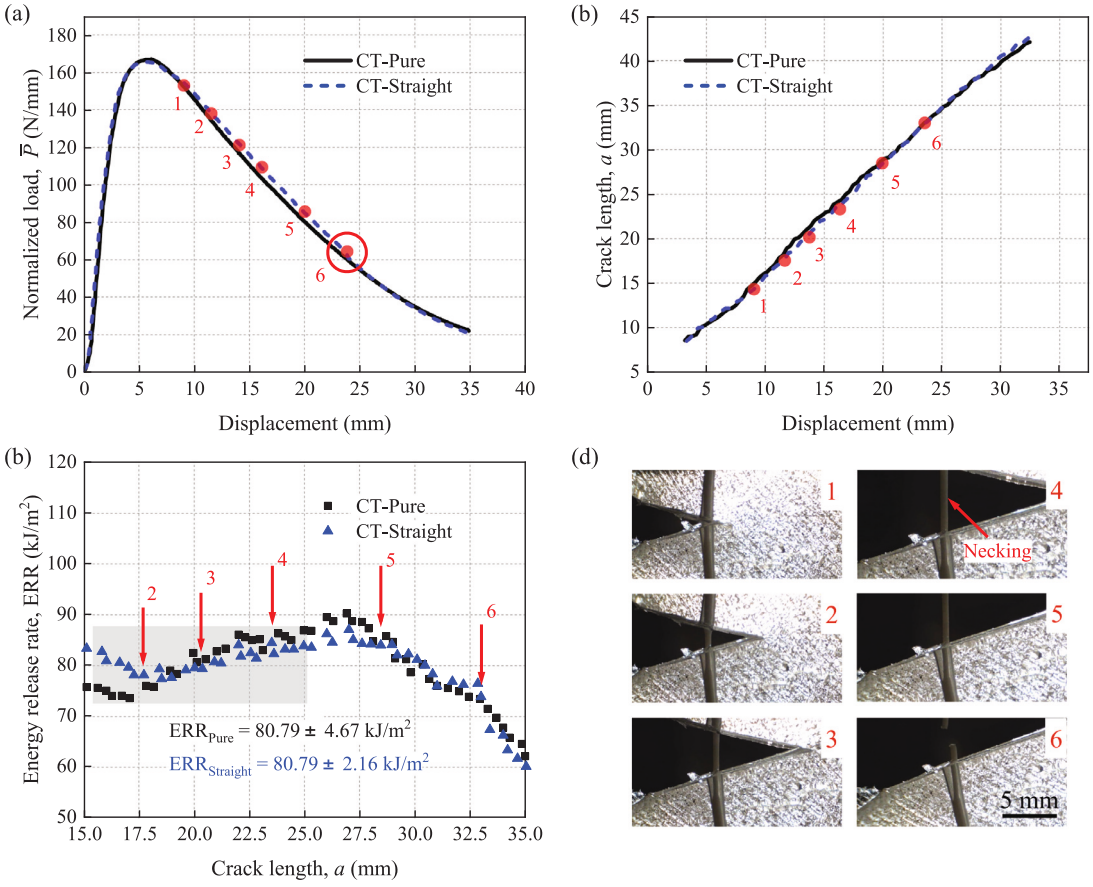

Fig. 5. Compact tension representative test results of PLA straight fiber in comparison with pure epoxy: (a) normalized load $\overline{P}$ versus displacement (the normalized load equals the value of load divided by the specimen's actual thickness), (b) crack length versus displacement, and (c) energy release rate versus crack length. The gray area in (c) outlines the region considered to calculate the average energy release rate: the range of reinforcement influence until the energy release rate starts to decline. (d) Images of the microscope close to the crack tip of the specimen CT-Straight from point 1 to 6. The red circle in (a) indicates the PLA straight fiber breaking position.

Parallel to this, as the crack reaches the position of OC (around crack length a = 15.5 mm), the sacrificial bond breaks and the hidden length of the curl starts to unfold. From this point, the load-capacity of the OC increases, allowing it to partially support the overall load in the CT specimen, and the OC bridging mechanism begins to take effect and contributes to the ERR improvement. As discussed in Section 3.3.1, the straight fiber in CT-Straight, as it does not have a hidden length, immediately shows necking and its load-capacity decreases. Therefore, its bridging effect is negligible and the ERR values remain the same as in CT-Pure. While both CT-OC_Z10 and CT-OC_Z5 show an increase in the ERR due to the existence of the overlapping curls.

Even though the shorter hidden length leads to the early break of OC_Z5, compared to OC_Z10 (after point 3 in Fig. 8(c) and (d)), CT-OC_Z5 exhibits better ERR improvement than OC_Z10. This is believed to be related with the formation of an epoxy ligament in CT-OC_Z5 only present on this specimen type as indicated by the arrow in Fig. 8(d)-point 2. The fracture surface images below the ERR plots give an illustration of this epoxy ligament phenomenon. From Fig. 8(a) and (b), it is clear that CT-Pure and CT-Straight have smooth fracture surfaces and their ERR values are comparable. In the fracture surfaces of CT-OC_Z10 (Fig. 7(c)), the surface is rougher before a = 25.2 mm because of the micro-cracks formation of the void and the ERR increases accordingly. But after crack length a = 25.2 mm, the fracture surface is as smooth as the above CT-Pure and CT-Straight specimens and the ERR values jump back to the CT-Pure. This epoxy ligament observed only on the CT-OC_Z5 might be related with crack twisting effects triggered by a small curl size OC. This crack twisting increases the ERR as it creates a crack branching and an increase on the fracture surface [39]. To better quantify this crack formation, Table 5 shows the surface roughness measured along three selected lines (i, ii, and (iii). The CT-Straight and CT-OC_Z10 show similar values of roughness. However, in CT-OC_Z5, especially after point 2 - Fig. 7(d), the epoxy ligament starts to form, which also leads to a rougher fracture surface (R_a = 383.1 ± 3.3 mm) throughout the crack path. Once the epoxy ligament is triggered from the end position of the curl of OC_Z5, it is further developed and leads to an extra toughening mechanism, subsequently delaying the crack propagation and improving the ERR.

Based on the experimental result and in-situ observations shown above, Fig. 9 summarizes the three main toughening mechanisms identified during crack propagation of CT-OC_Z5 specimen: void created by the curl of OC, OC bridging, and epoxy ligament. It is important to note that these three toughening mechanisms were only triggered when the crack initiation and crack propagation were constrained to pass through the OC. Nevertheless, it is assumed that by decreasing the dimensions of the 3D-printed OC, it will be possible to incorporate a larger number of fibers into the epoxy, and it will no longer be necessary to constrain crack initiation and propagation to a specific direction, as multiple OCs distributed throughout the epoxy matrix could activate at different locations and thereby improve the overall toughness. Confirming this assumption will be tested in future works.

4. Discussion

In the previous detailed analysis of the CT test results, it is concluded that the integration of the overlapping curl into the epoxy

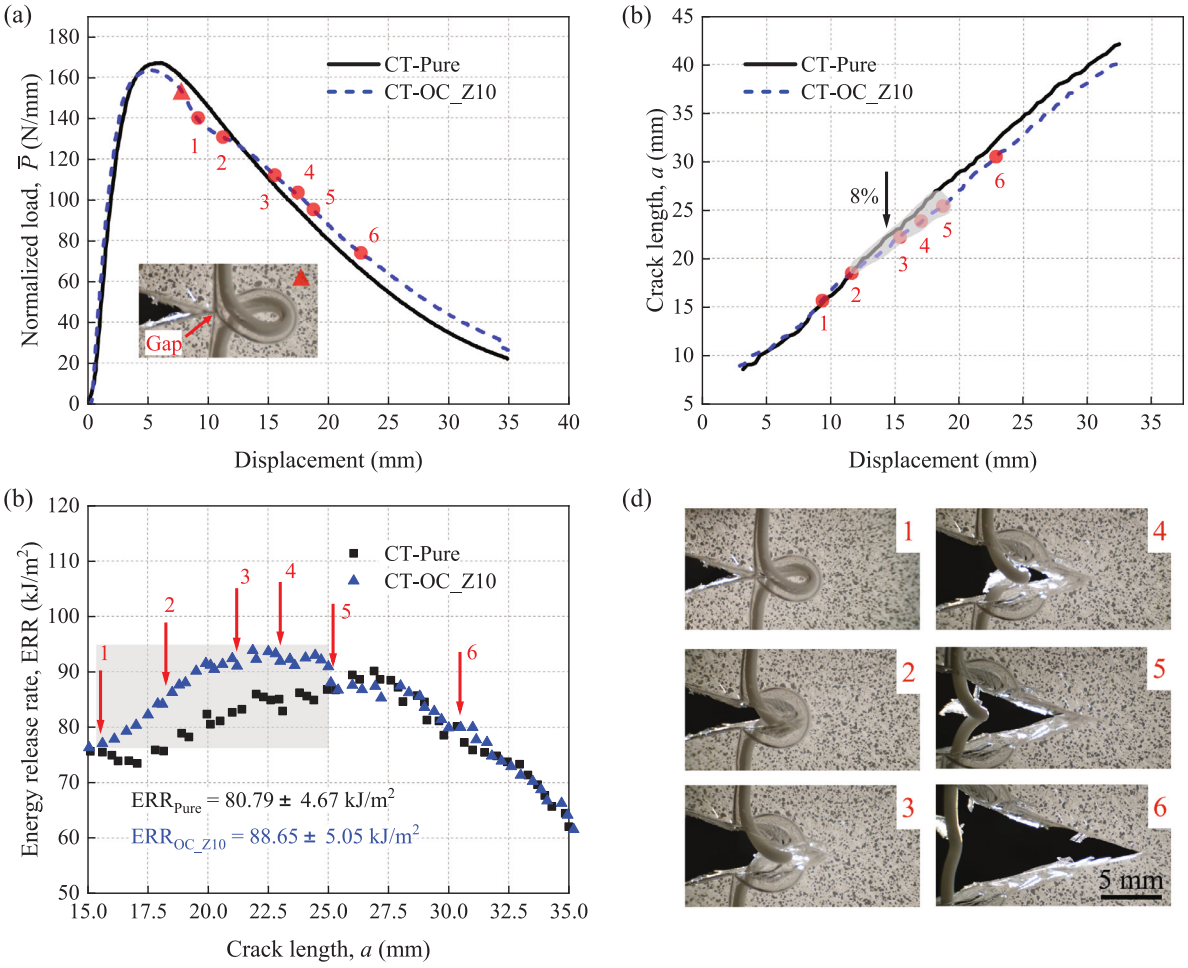

Fig. 6. Compact tension representative test results of PLA Z10 overlapping curl in comparison with pure epoxy: (a) normalized load $\overline{P}$ versus displacement (the normalized load equals the value of load divided by the specimen's actual thickness), (b) crack length versus displacement, and (c) energy release rate versus crack length. The gray area in (c) outlines the region considered to calculate the average energy release rate: the range of reinforcement influence until the energy release rate starts to decline. (d) Images of the microscope close to the crack tip of the specimen CT-OC_Z10 from point 1 to 6.

introduces complex toughening mechanisms, of which three could be identified: (1) void, (2) overlapping curl bridging, and (3) epoxy ligament. The last is only present when the OC_Z5 is integrated in the epoxy, while the first two occur on both OC-geometries. In order to better understand the role of each of these toughening mechanisms in the overall improvement of the crack resistance of the epoxy material, a finite element analysis has been performed in which each of the three toughening mechanisms is analyzed separately and compared with the pure epoxy case.

4.1. Numerical model

Fig. 10(a) shows the 3D Finite Element Model (FEM, thickness = 8 mm) built in ABAQUS 2021 to simulate the CT test, including the mesh and the boundary conditions. The geometry of the model follows the CT specimens geometry shown in Fig. 2(b). The eight-node brick elements (C3D8) were used to model the epoxy matrix, implementing the true stress–strain curve derived from Fig. 4. The crack propagation within the epoxy was simulated using the eight-node three-dimensional cohesive elements (COH3D8) with a finite thickness of 0.01 mm. A bi-linear traction separation law was implemented into the model to predict crack growth and degradation based on the MAXStress crack criterion. The stiffness of the cohesive elements was set to 1×10^5 N/mm. The traction and energy release rate values were chosen as 13 MPa and 70 kJ/m^2 to the best fit of the simulated normalized load versus displacement curve to the experimental result. The boundary conditions were applied to the reference points RP1 and RP2. The degrees of freedom in the *y*-direction of the front and back surfaces were constrained to avoid buckling. A mesh sensitivity was conducted and mesh size was chosen as 0.4 × 0.4 × 0.4 around the crack path and 0.4 × 0.8 × 0.4 in the other region.

Fig. 10(b) shows the comparison of the simulated normalized load versus displacement curves with the experimental results. While some discrepancies are observed in the detailed shape of the curves, the model accurately predicts the maximum load and the overall trend of the experimental curve and closely matches the experimental data. These findings demonstrate that the model is capable of capturing the key mechanical behaviors and is effective for the intended analysis of comparison of the three toughening mechanisms.

4.2. Void effects on CT load versus displacement curves and stress field

The void caused by the integration of the OC into the epoxy was simulated by removing the elements in a cylindrical shape from the center of the CT model, as shown in Fig. 11(a). The geometry of the cross-section of the cylinder for each OC-series is taken from the ellipse fitted along the edge of the void in Fig. 8(c) and (d). The voids start 5 mm away from the initial crack tip, where the OC is integrated in previous experimental tests. The void depths are assumed to be 4 mm and consistent for both the OC geometries. The void ellipse formed by

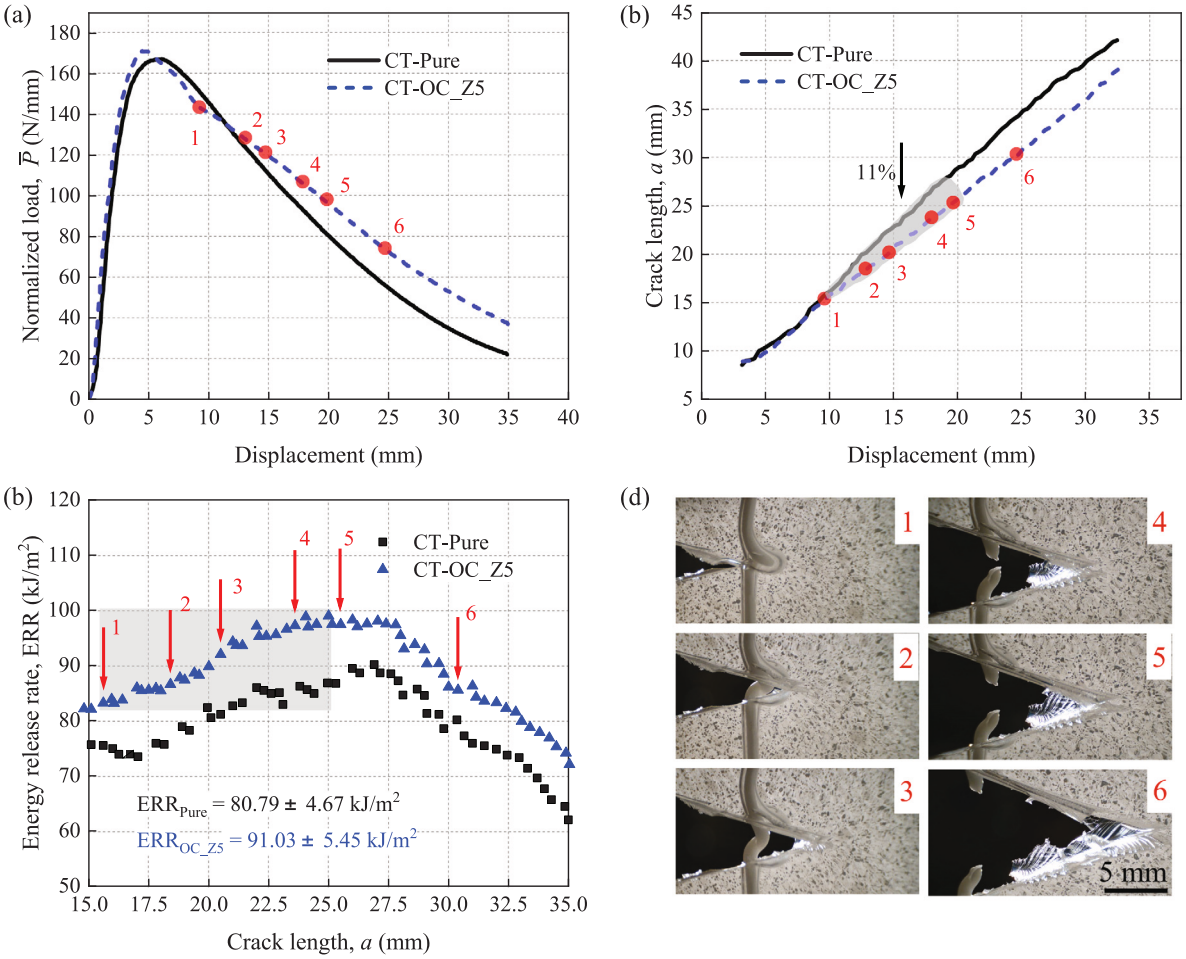

Fig. 7. Compact tension representative test results of PLA Z5 overlapping curl in comparison with pure epoxy: (a) normalized load $\overline{P}$ versus displacement (the normalized load equals the value of load divided by specimen's actual thickness), (b) crack length versus displacement, and (c) energy release rate versus crack length. The gray area in (c) outlines the region considered to calculate the average energy release rate: the range of reinforcement influence until the energy release rate starts to decline. (d) Images of the microscope close to the crack tip of the specimen CT-OC_Z5 from point 1 to 6.

OC_Z10 has a major axis length of 5.6 mm and a minor axis length of 2.4 mm, while the ellipse formed by OC_Z5 has a major axis length of 3.6 mm and a minor axis length of 2.4 mm.

Fig. 11(b), (c), and (d) show the results of the FEM. Comparing the load–displacement curves in Fig. 11(b), we can observe a decrease in the maximum load in the presence of the void. In addition, the load decrease in CT-Void-OC_Z10 is larger than CT-Void-OC_Z5 because of its larger void size. These observations are in accordance with the experimental results — see Figs. 6(a) and 7(a). Fig. 11(c) shows the section-view of stress field σ_{zz} in the epoxy matrix at the region of the void for both Void-models at the same critical displacement. Fig. 11(d) plots the stress σ_{zz} values along the red dashed arrow in Fig. 11(c). From the void's end corner "A", σ_{zz} affects a wider region of the epoxy in CT-Void-OC_Z5 than in CT-Void-OC_Z10, as shown by d_1 and d_2 on the double-headed arrow, indicating more epoxy material undergoes deformation in CT-Void-OC_Z5. We believe that a larger volume of material in deformation leads to more non-uniform stress distribution in the deformed material and is favorable to initiate micro-cracks, which promotes the corresponding epoxy ligament formation in the CT-OC_Z5.

4.3. Overlapping curl bridging effects on CT load versus displacement curve and stress field

To investigate the OC bridging effects on the epoxy matrix solely, a spring element with nonlinear behavior is used to reproduce the OC mechanical behavior, as shown in Fig. 12(a). Since the sacrificial bond breaks before the crack tip reaches it, we only reproduce the OC response afterwards, i.e., after F_h, 3.39 N and 10.66 N for OC_Z10 and OC_Z5, respectively. This is a simplified model of the OC bridging, intended to aid in understanding the key toughening mechanisms rather than to fully capture the fracture process.

Fig. 12(b) shows the load vs. displacement curves in comparison with CT-pure. A very small increase in the normalized load can be observed in the zoom-in of the peak load. Further on the displacement, around 20 mm, we can observe a drop in the load for the CT-Spring-OC_Z10. This is the position when the OC spring reaches F_u and no longer withstands any load. This drop shows the bridging effect of the OC. However, this effect is almost negligible in the peak load. As a result, the contribution of the OC bridging to the overall load of the CT is almost negligible. Fig. 12(c) shows the effect of the OC-bridging on the stress field σ_{zz} on the epoxy matrix, both for OC_Z10 and OC_Z5. The plots are taken at the same critical step, where the crack tip propagates ahead of the position of OC around crack length 18.19 mm. After the crack reaches the curl position, the holding force F_h starts to redistribute the stress field around the OC and subsequently affects the crack propagation. Because of the higher F_h value of 10.66 N of OC_Z5 in comparison with OC_Z10, the OC_Z5 affects the stress field more than the OC_Z10, causing more significant stress redistribution at the OC position. This larger effect on the stress field for OC_Z5 possibly enlarges the fracture process zone and might be one of the causes why

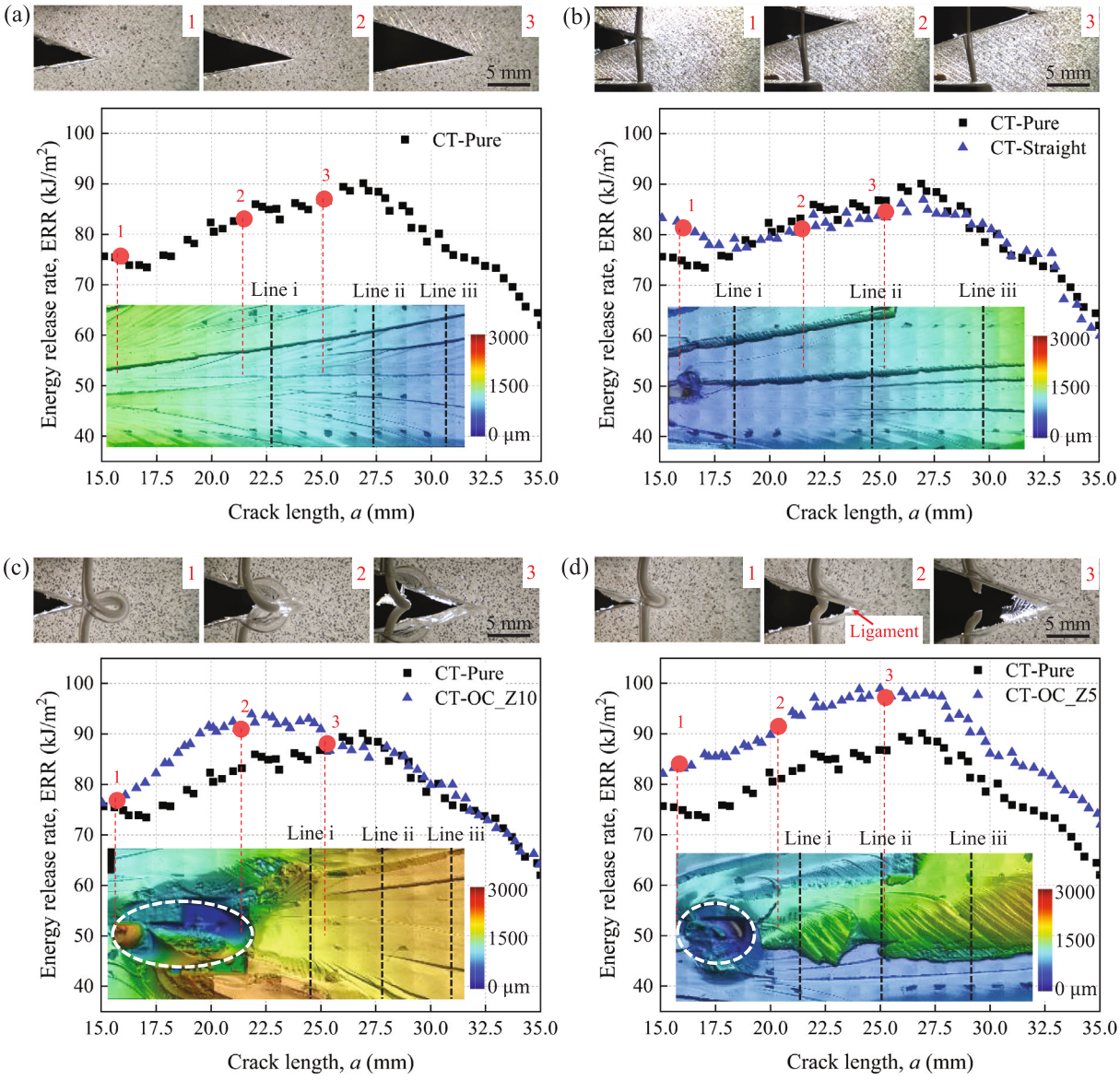

Fig. 8. In-situ optical observations of the fracture process, corresponding energy release rate data points, and the 3D fracture surfaces (shown in 2D view) for (a) CT-Pure, (b) CT-Straight, (c) CT-OC_Z10, and (d) CT-OC_Z5. The height scales next to fracture surface images indicate the surface topography. The white dashed ellipses outline the void created by the curl of OC. The black dashed lines i, ii, and iii indicate the selected fracture surface roughness measurement profiles.

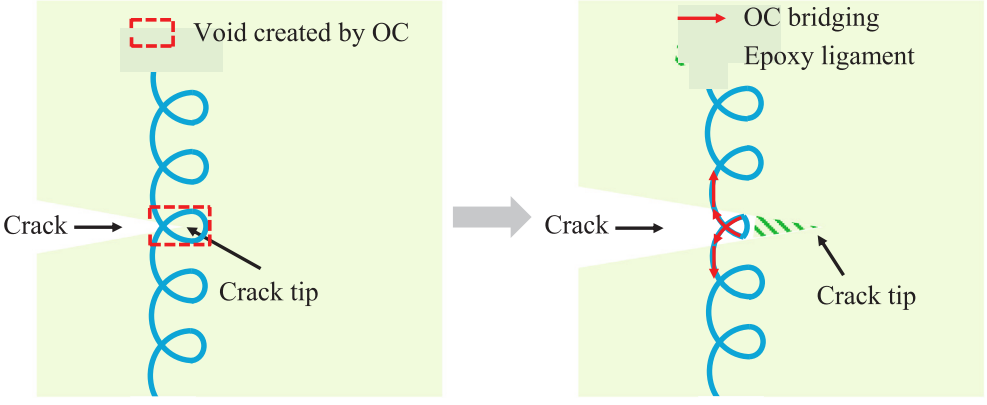

Fig. 9. Schematic of toughening mechanisms during the crack propagation in the CT-OC_Z5: void created by the curl, OC bridging, and epoxy ligament.

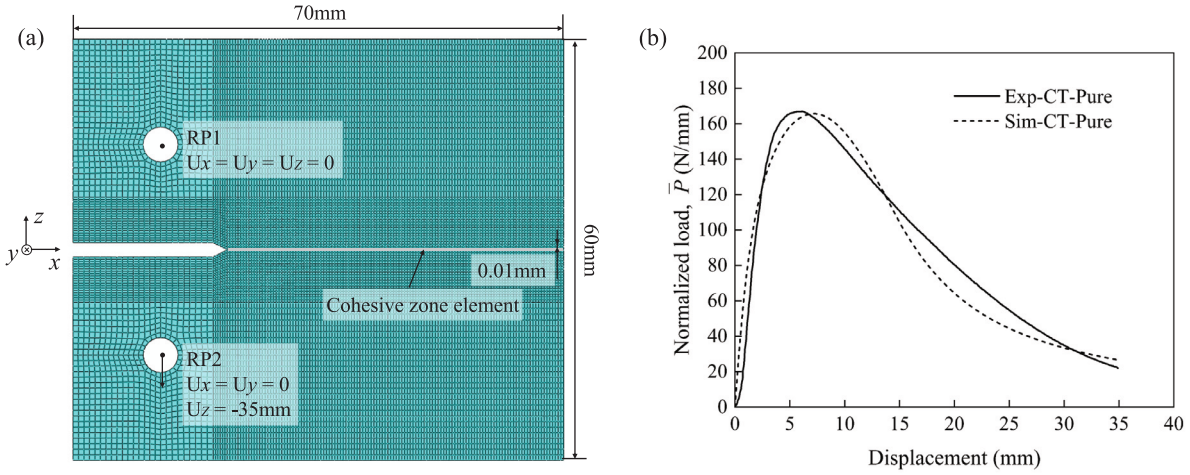

Fig. 10. (a) Geometry, boundary conditions, and corresponding mesh of the pure compact tension finite element model. The detailed compact tension geometry can be found in Fig. 2(b). (b) Comparison of the experimental and simulated normalized load versus displacement curves of pure compact tension specimen.

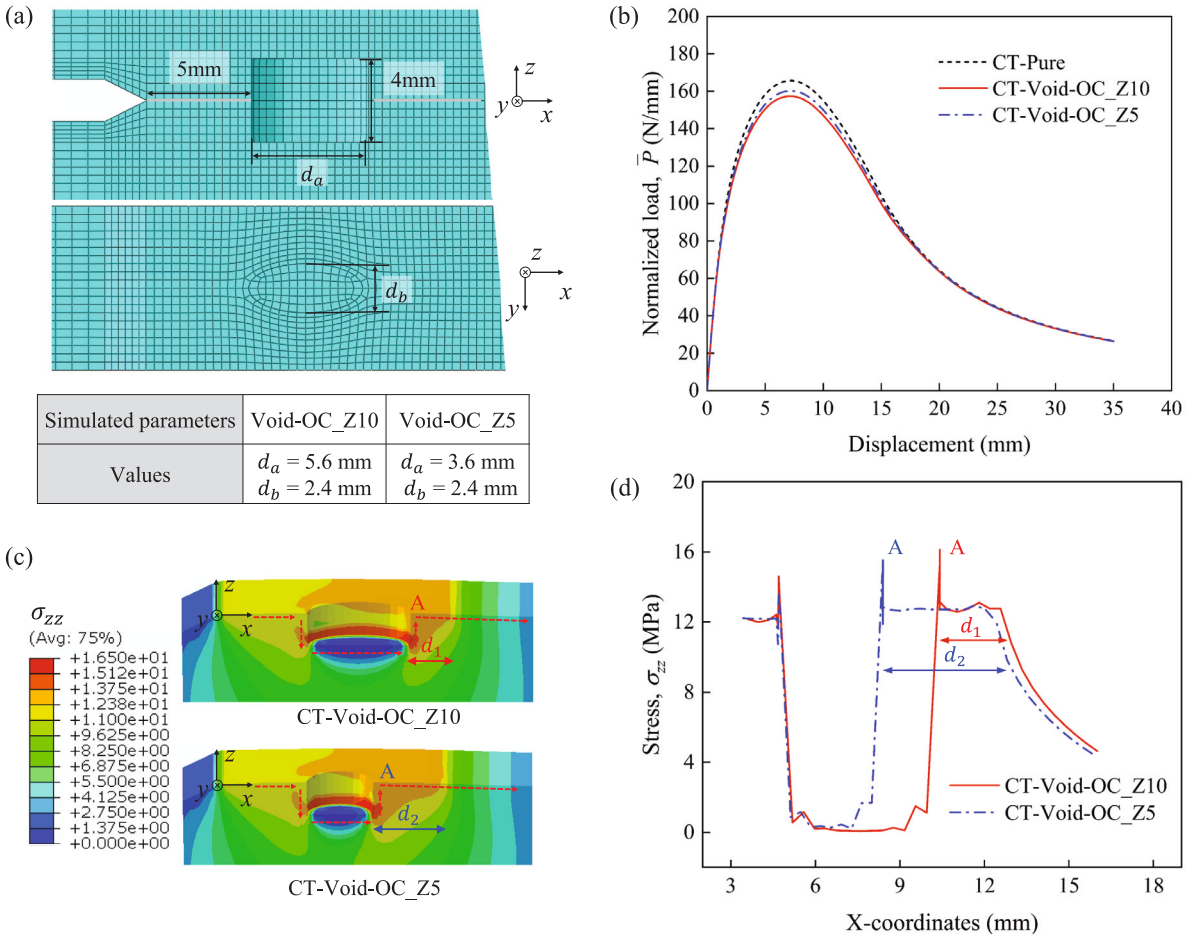

Simulated parameters	Void-OC_Z10	Void-OC_Z5
Values	d_a = 5.6 mm d_b = 2.4 mm	d_a = 3.6 mm d_b = 2.4 mm

Fig. 11. (a) Compact tension finite element model simulating the void created by the embedded overlapping curl and corresponding geometry. (b) Comparison of the numerical normalized load versus displacement curves of compact tension specimens without void (CT-Pure) and with two void sizes, one corresponding to the void size of CT-OC_Z10 (CT-Void-OC_Z10) and the other corresponding to the void size of CT-OC_Z5 (CT-Void-OC_Z5). (c) Stress component σ_{zz} field in the section view of CT specimens with the voids at the same critical displacement. The red dashed line shows the path for the extracted σ_{zz} values in (d). In (c) and (d), "A" indicates the end corner of the void. The double-headed arrows represent the lengths d_1 and d_2 of the region of the epoxy material under deformation, located beyond the end corner of the void.

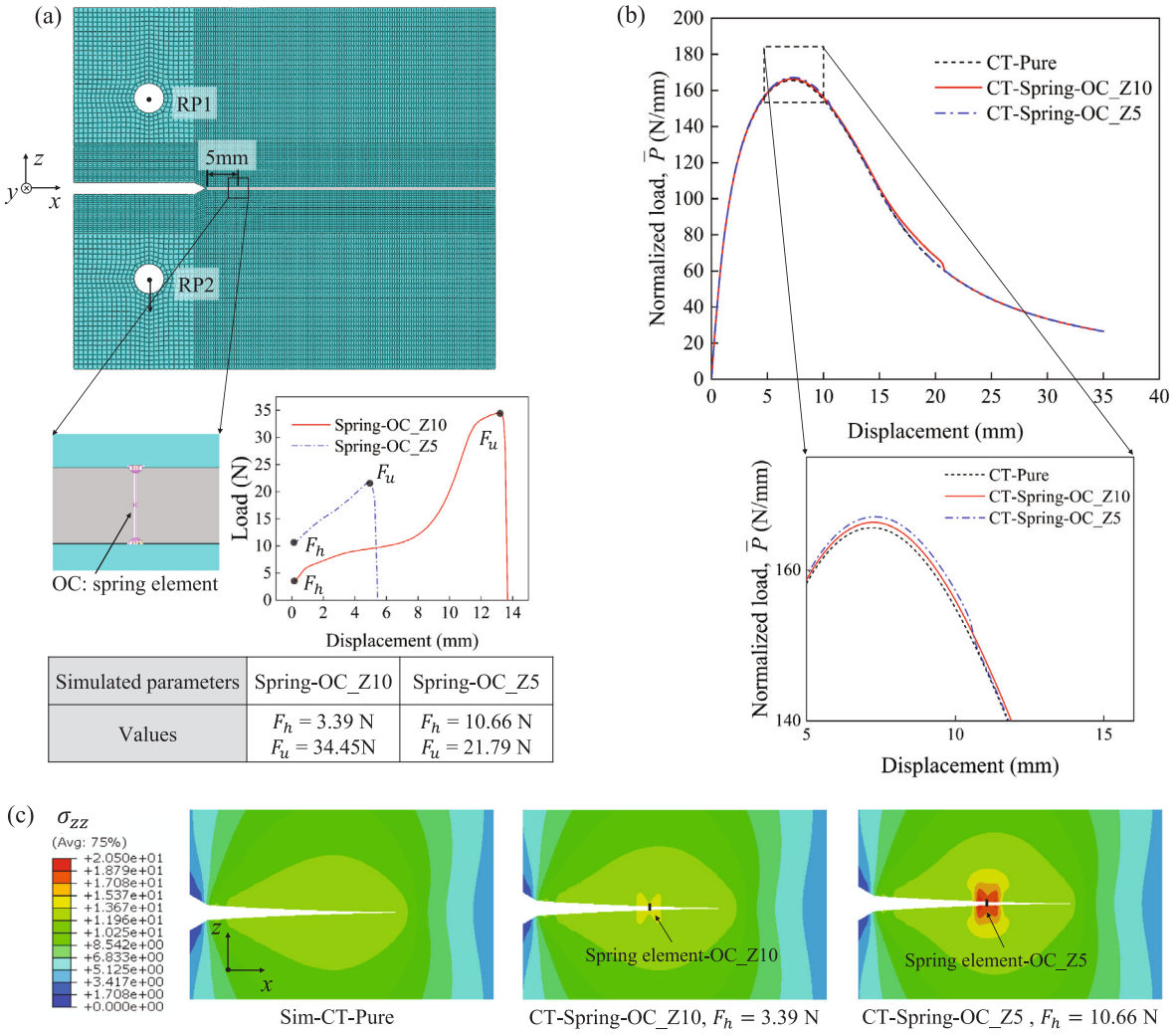

Simulated parameters	Spring-OC_Z10	Spring-OC_Z5
Values	F_h = 3.39 N F_u = 34.45N	F_h = 10.66 N F_u = 21.79 N

Fig. 12. (a) Compact tension finite element model with a spring element to simulate the bridging effect of the embedded overlapping curl. The inset figure is the input OC load versus displacement curve simulated by the spring element to reproduce the OC bridging. (b) Numerical normalized load versus displacement curves of pure CT and CT with Spring-OC element. (c) Stress field σ_{zz} induced by the spring-OC element when F_h is achieved at crack length of a = 18.19 mm.

an epoxy ligament has the tendency to form for OC_Z5 and not for OC_Z10.

4.4. Epoxy ligament effect on the CT load versus displacement response

As discussed in the previous sub-section (Sections 4.2 and 4.3), the voids and OC-bridging might have an important role in triggering the crack deflection and epoxy ligament formation. Specifically for OC_Z5, the smaller void size and larger F_h modified the stress field to a larger extent ahead of the OC, which could contribute to the epoxy ligament formation in CT-OC_Z5. To show the epoxy ligament effect on the CT mechanical response, the ligament is simulated in the CT-Pure model by a region in the cohesive layer that exhibits higher ERR, as shown in Fig. 13(a). Since only CT-OC_Z5 shows the epoxy ligament, the starting position of the ligament region is determined by the end of the corresponding void: 8.6 mm from the initial crack tip. As definitive parameters of the ligament are difficult to identify, values were varied within a range to identify their effect on the overall load. Parameters regarding the ligament region length L = 8, 12, 16 mm and ERR values $\mathrm{ERR}_{\mathrm{ligament}}$ = 90, 100 kJ/m^2 are studied for the normalized load versus displacement response of the CT simulation.

In Fig. 13(b), a significant influence is identified on the load–displacement curves after the peak load. Similar behavior is also observed in Fig. 7(a) - CT-OC_Z5, where a ligament is experimentally observed. The ligament can significantly affect the CT load capacity. The longer ligament region L and the higher ligament $\mathrm{ERR}_{\mathrm{ligament}}$, the larger will be the increase in the load.

4.5. "Strong" overlapping curl bridging effect on the CT energy release rate ratio

Based on the previous numerical results, we can conclude that one of the major contributions to the increase of the ERR of the CT-OC_Z5 observed in the experiments is due to the ligament formation, the overlapping curl structure and its mechanical behavior is crucial to trigger the epoxy ligament, as shown in the stress field σ_{zz} both for the void and OC-bridging. Nevertheless, since the CT-Pure peak load is 39 times higher than the F_u of one single curl (OC_Z10, F_u = 34.45 N), it is important to understand whether a higher OC F_u could significantly enlarge the contribution of the OC bridging to the ERR enhancement. With increasing F_u of the OC, it is expected to increase the load response in the CT. In order to understand if this would hold true, a "stronger" OC was simulated by applying a scaling factor to increase the load-capacity for OCZ5 and OCZ10 while maintaining the displacement of the spring OC. The load versus displacement curves of these "stronger" OCs are plotted in Fig. 14(a). As a result, the ultimate load F_u of these strong OC_Z10 and OC_Z5 achieves approximately the same magnitude but with different hidden lengths.

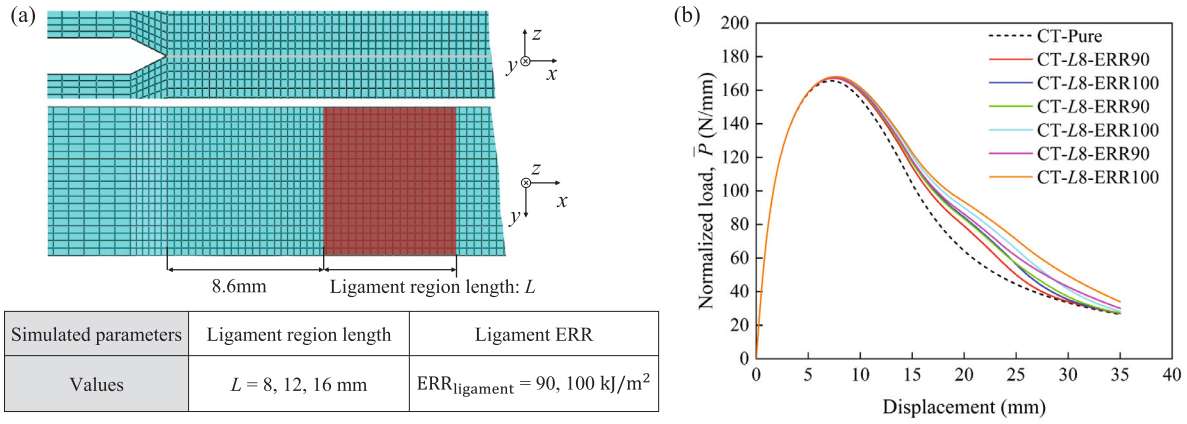

Simulated parameters	Ligament region length	Ligament ERR
Values	L = 8, 12, 16 mm	$ERR_{ligament}$ = 90, 100 kJ/m^2

Fig. 13. (a) Compact tension finite element model considering the epoxy ligament region and its corresponding energy release rate on (b) the normalized load versus displacement curves. The ligament region is located 8.6 mm from the crack tip, just beyond the end corner of the void geometry.

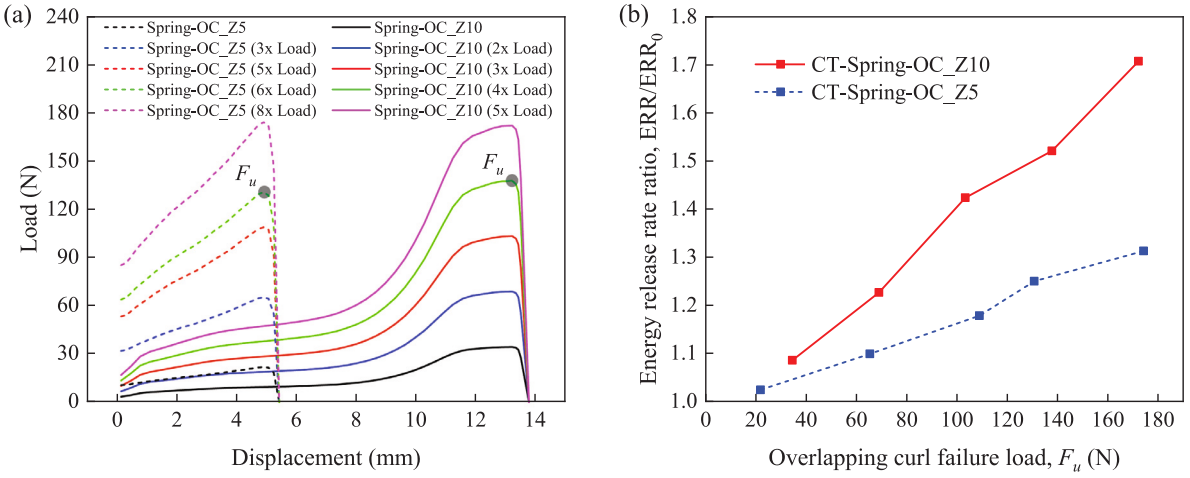

Fig. 14. (a) The input load versus displacement curves of overlapping curl simulated by spring element to produce OC bridging effect. The failure load F_u of Spring-OC_Z10 and Spring-OC_Z5 are adjusted by applying a scaling factor to achieve approximately the same magnitude. (b) The Spring-OC_Z10 and Spring-OC_Z5 bridging effects on the energy release rate ratio, ERR/ERR$_0$, with the increased overlapping curl failure load. ERR represents the energy release rate in CT-Spring-OC simulations at the crack length where the OC breaks and the failure load F_u is reached. ERR$_0$ refers to the energy release rate in CT-Pure results at the same crack length.

Fig. 14(b) shows the results of the "stronger" OC CT-simulations by plotting the ERR/ERR$_0$ as a function of the OC F_u. The ERR value is taken at crack length where the F_u is reached — just before OC breaks, while ERR$_0$ is the ERR at the same crack length but taken from the CT-Pure. It is evident that as the F_u increases, the ratio ERR/ERR$_0$ increases accordingly, indicating a progressively bridging effect. In addition, the hidden length plays an important role in the bridging effect. The shorter hidden length of OC_Z5 causes it to break prematurely during the crack propagation process, limiting its bridging effect. Contrary to this, the OC_Z10 with longer hidden length shows a higher ERR/ERR$_0$ value than OC_Z5 at the same F_u value. From Fig. 14, we see that with "stronger" overlapping curls, the OC bridging effect becomes more significant. This indicates that new materials and technologies are worth investigating to manufacture OCs with a stiffer response and higher failure load to further explore the OC-toughening mechanisms in the epoxy matrix. Moreover, advances that allow the fabrication of smaller OCs would make it possible to incorporate a larger number of fibers into the epoxy, permitting their simultaneous activation and ultimately improving the overall fracture toughness.

5. Conclusions

In this work, a novel design by impregnating a bio-inspired overlapping curl structure, consisting of sacrificial bonds and hidden lengths, into a bio-based epoxy is proved to be able to improve the epoxy fracture resistance. Three key mechanisms are identified and analyzed that underpin the observed toughening effect: (1) crack re-initiation created by the void, (2) OC bridging effect, and (3) epoxy ligament, which delayed crack propagation and improved energy release rate by up to 13%.

The experimental results showed that the hidden length topology feature is crucial for the increase in toughness, as the crack propagation and ERR of the epoxy with the straight fiber remain the same as in the pure specimen (no reinforcement).

The impregnated OC triggers complex fracture processes. As revealed by the in-situ observation, after the crack passes through the OC, the crack needs to re-initiate after passing the void created by the OC. Then, the OC exhibits a bridging effect due to the hidden length unfolding after the sacrificial bond break. For smaller hidden lengths, the local stress redistribution caused by the OC bridging can enlarge the

fracture process zone, and promote the formation of epoxy ligament, possibly related with crack branching. The epoxy ligament plays the most significant role in the ERR improvement in CT-OC_Z5.

The curl geometry and mechanical properties are important characteristics of the overlapping curl, which are also essential for the epoxy ligament formation. The OC_Z5 with a smaller curl size shows a higher holding force 10.7 N, causing more pronounced local stress field redistribution and enlarging the fracture process zone ahead of the crack tip when compared to OC_Z10. This might have an effect on the triggering of the epoxy ligament, which delays the crack propagation by 11% and improves ERR up to 13%.

This paper proves the concept of using the 3D-printed overlapping curls structure to toughen the bio-based epoxy, despite the limited improvement in ERR to a 13% increase. This limitation arises from the high ERR values (80.8 kJ/mm^2), attributed to the large plastic dissipation energy of the epoxy, compared with the relatively low overlapping curl load-capacity (34.5 N). From the parametric study using FEM, an OC with a higher failure load can achieve a higher bridging effect. In addition, considering only the OC bridging effect without any epoxy ligament effect, FEM simulation shows that the overlapping curl with a longer hidden length is more effective in increasing the energy release rate than the shorter hidden length.

CRediT authorship contribution statement

Zhiyuan Xu: Writing – original draft, Visualization, Methodology, Data curation, Conceptualization. **Ran Tao:** Writing – review & editing, Visualization, Validation, Supervision, Methodology, Data curation, Conceptualization. **Kunal Masania:** Writing – review & editing, Visualization, Supervision, Methodology, Conceptualization. **Sofia Teixeira de Freitas:** Writing – review & editing, Visualization, Validation, Supervision, Methodology, Investigation, Conceptualization.

Declaration of competing interest

The authors declare the following financial interests/personal relationships which may be considered as potential competing interests: Sofia Teixeira de Freitas reports financial support was provided by Foundation for Science and Technology. Zhyiuan Xu reports financial support was provided by China Scholarship Council. If there are other authors, they declare that they have no known competing financial interests or personal relationships that could have appeared to influence the work reported in this paper.

Acknowledgments

The authors gratefully acknowledge the financial support from the China Scholarship Council (No. CSC202107720061). This work is also supported by Fundação da Ciência e Tecnologia (FCT), through IDMEC, under LAETA, project UIDB/50022/2020.

Data availability

The Data is available on the DOI: https://doi.org/10.4121/ff4882ad-4cd6-49d3-8878-623c6b712759.

References

[1] R. Lima, R. Tao, A. Bernasconi, M. Carboni, N. Carrere, S. Teixeira de Freitas, Uncovering the toughening mechanisms of bonded joints through tailored CFRP layup, Compos. Part B: Eng. 263 (2023) 110853.
[2] J.S. Jayan, A. Saritha, K. Joseph, Innovative materials of this era for toughening the epoxy matrix: a review, Polym. Compos. 39 (S4) (2018) E1959–E1986.
[3] D.E. Anastasiou, A sustainable alternative? A comparative life cycle assessment of epoxy adhesives, J. Appl. Polym. Sci. 140 (48) (2023) e54725.
[4] H.-Y. Tsai, Y. Nakamura, T. Fujita, M. Naito, Strengthening epoxy adhesives at elevated temperatures based on dynamic disulfide bonds, Mater. Adv. 1 (9) (2020) 3182–3188.
[5] M. Baig, M.A. Samad, Epoxy\epoxy composite\epoxy hybrid composite coatings for tribological applications—a review, Polymers 13 (2) (2021) 179.
[6] J. Dai, Y. Peng, N. Teng, Y. Liu, C. Liu, X. Shen, S. Mahmud, J. Zhu, X. Liu, High-performing and fire-resistant biobased epoxy resin from renewable sources, ACS Sustain. Chem. Eng. 6 (6) (2018) 7589–7599.
[7] R. Xie, Y. Yuan, P. Sun, Z. Liu, J. Ma, G. Yang, K. Wang, M. Li, L. Shang, Y. Ao, Design of epoxy resin with sustainability, high adhesion and excellent flame retardancy based on bio-based molecules, J. Mater. Sci. 57 (27) (2022) 13078–13096.
[8] S. Nikafshar, O. Zabihi, S. Hamidi, Y. Moradi, S. Barzegar, M. Ahmadi, M. Naebe, A renewable bio-based epoxy resin with improved mechanical performance that can compete with DGEBA, RSC Adv. 7 (14) (2017) 8694–8701.
[9] M.N. Saleh, N.Z. Tomic, A. Marinkovic, S. Teixeira de Freitas, The effect of modified tannic acid (TA) eco-epoxy adhesives on mode I fracture toughness of bonded joints, Polym. Test. 96 (2021) 107122.
[10] N.Z. Tomic, M.N. Saleh, S. Teixeira de Freitas, A. Zivkovic, M. Vuksanovic, J.A. Poulis, A. Marinkovic, Enhanced interface adhesion by novel eco-epoxy adhesives based on the modified tannic acid on Al and CFRP adherends, Polymers 12 (2020) 1541.
[11] R.O. Ritchie, The conflicts between strength and toughness, Nat. Mater. 10 (11) (2011) 817–822.
[12] U.G. Wegst, H. Bai, E. Saiz, A.P. Tomsia, R.O. Ritchie, Bioinspired structural materials, Nat. Mater. 14 (1) (2015) 23–36.
[13] H. Hsieh, A. Kinloch, K. Masania, A. Taylor, The mechanisms and mechanics of the toughening of epoxy polymers modified with silica nanoparticles, Polymer 51 (2010) 6284–6294.
[14] C. van Innis, M.K. Budzik, T. Pardoen, Bridging in co-cured composite joints, Int. J. Solids Struct. (2024) 113194.
[15] Y. He, K. Duan, L. Yao, J. Tang, J. Zhang, D. Jiang, Q. Liu, Y. Lu, Synergistic toughening on CFRP via in-depth stitched CNTs, Compos. Part B: Eng. 254 (2023) 110605.
[16] A. Wagih, R. Tao, G. Lubineau, Bio-inspired adhesive joint with improved interlaminar fracture toughness, Compos. Part A: Appl. Sci. Manuf. 149 (2021) 106530.
[17] R. Tao, X. Li, A. Yudhanto, M. Alfano, G. Lubineau, Laser-based interfacial patterning enables toughening of CFRP/epoxy joints through bridging of adhesive ligaments, Compos. Part A: Appl. Sci. Manuf. 139 (2020) 106094.
[18] R.B. Ladani, A.R. Ravindran, S. Wu, K. Pingkarawat, A.J. Kinloch, A.P. Mouritz, R.O. Ritchie, C.H. Wang, Multi-scale toughening of fibre composites using carbon nanofibres and z-pins, Compos. Sci. Technol. 131 (2016) 98–109.
[19] M. Li, S. Li, J. Xiao, Y. Fu, W. Zhu, Y. Ke, An integrated nanofiller spray and nanosecond pulse electrically-assisted method for synergistically interlaminar toughening and in-situ damage monitoring of CFRP composites, Compos. Part B: Eng. 275 (2024) 111355.
[20] A. Wagih, G. Lubineau, Enhanced mode II fracture toughness of secondary bonded joints using tailored sacrificial cracks inside the adhesive, Compos. Sci. Technol. 204 (2021) 108605.
[21] A. Ghareeb, A. Elbanna, Extreme enhancement of interfacial adhesion by bulk patterning of sacrificial cuts, Extrem. Mech. Lett. 28 (2019) 22–30.
[22] Y. Shao, H.-P. Zhao, X.-Q. Feng, H. Gao, Discontinuous crack-bridging model for fracture toughness analysis of nacre, J. Mech. Phys. Solids 60 (8) (2012) 1400–1419.
[23] B. Schmuck, G. Greco, T.B. Pessatti, S. Sonavane, V. Langwallner, T. Arndt, A. Rising, Strategies for making high-performance artificial spider silk fibers, Adv. Funct. Mater. 34 (35) (2024) 2305040.
[24] H. Li, C. Liu, J. Zhu, J. Sun, X. Huan, H. Geng, T. Li, L. Ge, X. Jia, X. Yang, et al., Spider silk-inspired heterogeneous interphase featuring hybrid interaction for simultaneously improving the interfacial strength and fracture toughness between carbon fiber and epoxy by regulating hydrogen bond density, Compos. Part B: Eng. 280 (2024) 111476.
[25] M.G. Mazzotta, A.A. Putnam, M.A. North, J.J. Wilker, Weak bonds in a biomimetic adhesive enhance toughness and performance, J. Am. Chem. Soc. 142 (10) (2020) 4762–4768.
[26] C. Houriet, B. Ulyanov, J.-A. Pascoe, K. Masania, Wood-inspired interlocking junctions using 3D-printed liquid crystal polymers, Addit. Manuf. 97 (2025) 104590.
[27] Z. Yin, F. Hannard, F. Barthelat, Impact-resistant nacre-like transparent materials, Science 364 (6447) (2019) 1260–1263.
[28] H. Wan, N. Leung, S. Algharaibeh, T. Sui, Q. Liu, H.-X. Peng, B. Su, Cost-effective fabrication of bio-inspired nacre-like composite materials with high strength and toughness, Compos. Part B: Eng. 202 (2020) 108414.
[29] S. Zou, D. Therriault, F.P. Gosselin, Spiderweb-inspired, transparent, impact-absorbing composite, Cell Rep. Phys. Sci. 1 (11) (2020).
[30] S. Zou, D. Therriault, F.P. Gosselin, Failure mechanisms of coiling fibers with sacrificial bonds made by instability-assisted fused deposition modeling, Soft Matter 14 (48) (2018) 9777–9785.
[31] Z. Xu, R. Tao, K. Masania, S. Teixeira de Freitas, Biomimetic toughening design of 3D-printed polymeric structures: Enhancing toughness through sacrificial bonds and hidden lengths, Mater. Des. 247 (2024) 113361.

[32] S. Zou, D. Therriault, F.P. Gosselin, Toughening elastomers via microstructured thermoplastic fibers with sacrificial bonds and hidden lengths, Extrem. Mech. Lett. 43 (2021) 101208.
[33] N.M. Ribe, M. Habibi, D. Bonn, Liquid rope coiling, Annu. Rev. Fluid Mech. 44 (1) (2012) 249–266.
[34] SICOMIN composites, technical datasheet, SR GreenCast 160 / SD 7160 clear casting resin system, 2023, URL https://www.sicomin.com.
[35] ISO 527-plastics – determination of tensile properties – part 2: Test conditions for moulding and extrusion plastics, 2012.
[36] M.N. Saleh, M.K. Budzik, M. Saeedifar, D. Zarouchas, S. Teixeira de Freitas, On the influence of the adhesive and the adherend ductility on mode I fracture characterization of thick adhesively-bonded joints, Int. J. Adhes. Adhes. 115 (2022) 103123.
[37] ASTM D5045. standard test method for plane-strain fracture toughness and strain energy release rate of plastic materials, 2014.
[38] M. Laffan, S. Pinho, P. Robinson, L. Iannucci, Measurement of the in situ ply fracture toughness associated with mode I fibre tensile failure in FRP. Part I: Data reduction, Compos. Sci. Technol. 70 (4) (2010) 606–613.
[39] N. Suksangpanya, N.A. Yaraghi, R.B. Pipes, D. Kisailus, P. Zavattieri, Crack twisting and toughening strategies in Bouligand architectures, Int. J. Solids Struct. 150 (2018) 83–106.